King Saud University

Arabian Journal of Chemistry

www.ksu.edu.sa
www.sciencedirect.com

ORIGINAL ARTICLE

Photocatalytic activity of nitrogen and copper doped TiO$_2$ nanoparticles prepared by microwave-assisted sol-gel process

CrossMark

S.M. Reda [a,*], **M. Khairy** [a,b], **M.A. Mousa** [a]

[a] Chemistry Department, Faculty of Science, Benha University, Benha, Egypt
[b] Chemistry Department, College of Science, Al Imam Muhammad Ibn Saud Islamic University, Saudi Arabia

Abstract Cu and N-doped TiO$_2$ photocatalysts were synthesized from titanium (IV) isopropoxide via a microwave-assisted sol-gel method. The synthesized materials were characterized by X-ray diffraction, UV-vis diffuse reflectance, photoluminescence (PL) spectroscopy, SEM, TEM, FT-IR, Raman spectroscopy, photocurrent measurement technique, and nitrogen adsorption–desorption isotherms. Raman spectra and XRD showed an anatase phase structure. The SEM and TEM images revealed the formation of an almost spheroid mono disperse TiO$_2$ with particle sizes in the range of 9-17 nm. Analysis of N$_2$ isotherm measurements showed that all investigated TiO$_2$ samples have mesoporous structures with high surface areas. The optical absorption edge for the doped TiO$_2$ was significantly shifted to the visible light region. The photocurrent and photocatalytic activity of pure and doped TiO$_2$ were evaluated with the degradation of methyl orange (MO) and methylene blue (MB) solution under both UV and visible light illumination. The doped TiO$_2$ nanoparticles exhibit higher catalytic activity under each of visible light and UV irradiation in contrast to pure TiO$_2$. The photocatalytic activity and photocurrent ability of TiO$_2$ have been enhanced by doping of the titania in the following order: (Cu, N) - codoped TiO$_2$ > N-doped TiO$_2$ > Cu-doped TiO$_2$ > TiO$_2$. COD result for (Cu, N)-codoped TiO$_2$ reveals ~92% mineralization of the MO dye on six h of visible light irradiation.

* Corresponding author.
  E-mail address: safenazr@yahoo.com (S.M. Reda).
Peer review under responsibility of King Saud University.

Production and hosting by Elsevier

1. Introduction

The photocatalysis origin is grounded on the excitation of electrons by light. Under the exploit of photons, the semiconductor creates highly oxidizing free radicals permitting the damage of materials adsorbed on its surface. Among the semiconductors listed in the literature, TiO$_2$ has been demonstrated most proper for most public environmental applications. This is attributed to its electronic and optical

properties, low cost, non-toxicity, high stability, and high efficiency in the degradation of environmental pollutants in air and water (Schneider et al., 2014). TiO$_2$ exhibits broad bandgap (3.0 eV for rutile and 3.2 eV for anatase) which restricts its light absorption to the only ultraviolet region. Consequently, pure TiO$_2$ works as a photocatalytic material under UV light (4–5% of solar light), but it has very low photocatalytic activity in visible light ($\sim$45% of solar spectrum). This restricts the real applications of TiO$_2$ as a photocatalyst and in the solar light collecting (Schneider et al., 2014; Dong et al., 2015; Kumar and Devi, 2011).

Numerous tactics have been made in the area of visible-light-active TiO$_2$ by incorporating different dopants into its crystal lattice, involving metal (Ag, Ni, Fe, Co) Ashkarran, 2011; Wang et al., 2014 and nonmetal elements (C, N, S, F) Szkoda et al., 2016; Wei et al., 2014; Zhai et al., 2014; Zhu et al., 2015. Theoretically, it was found that the p-orbitals of this dopant element extensively overlapped to facilitate the transference of photo-generated charge carriers to the surface of TiO$_2$ and consequently increase its photocatalytic activity (Yang et al., 2009).

The present work is designed to study the effect of introducing N and Cu as doping ions into TiO$_2$ lattice to increase its photocatalytic activity by producing electronic trapping sites. These sites will increase the hole lifetime producing during the photocatalytic reaction and consequently the probability to reach the surface without undergoing recombination to contribute in the reaction. The tested samples were synthesized using a microwave assisted sol-gel method. This method has attracted much consideration in recent years due to its numerous benefits such as unique synthetic paths, fast heating rates, short processing periods, uniformity and low power requirements (Komarneni et al., 1988). The usage of microwave irradiation is a potential way not only due to faster heating, but it also offers internal uniform heating developing into uniformly distributed mono dispersed particles.

This method may decrease the calcination time at the high calcination temperature. We discuss the textural surface properties, morphological and crystal phase structures as well as optical properties. The photocatalytic activities were also tested using model pollutants MB and MO dyes under each of UV and visible light irradiation. The use of (Cu,N)-codoped TiO$_2$ to determine COD has been studied.

2. Experimental

2.1. Sample preparation

All chemicals used were analytical-grade reagents.

Pure TiO$_2$ was prepared with double techniques including sol-gel and microwave approach. In a typical experiment, 40 ml of titanium (IV) isopropoxide was hydrolyzed in 500 ml water containing 6 ml nitric acid. The precipitated material produced was stirred to form a highly dispersed sol, which was then aged for 40 h and dried in a microwave oven operated at 1000 W and 2450 MHz for 30 min. The powder product was then calcined at 450 °C for 3 h. The sample was denoted as T.

N-doped TiO$_2$, Cu-doped TiO$_2$, and Cu.N-codoped TiO$_2$ were also fabricated by a double technique including sol–gel approach and microwave heating. Ammonium nitrate was utilized as a raw source of N dopants, which can produce a lot of gasses during the heating process. The evolved gasses are important to form the mesoporous structure. Similar to the procedure mentioned above, we added 3.68 g ammonium nitrate or 0.215 g Cu(NO$_3$)$_2$·3H$_2$O after the formation of the sol and keeping the microwave drying, and calcination steps as that mentioned before. The powders produced were denoted as NT and CuT for N-doped TiO$_2$ and Cu-doped TiO$_2$, respectively.

For preparing (Cu,N)-codoped TiO$_2$, 75 ml of 0.1 M Cu(NO$_3$)$_2$·3H$_2$O aqueous solution was added to 3 g of the as-synthesized N-doped TiO$_2$ placed in a ceramic crucible and stirred for 30 min. and then placed into a microwave oven operated at 1000 W and 2450 MHz for 30 min. The dried powder was finally calcined at 450 °C. The product, (Cu,N)-codoped TiO$_2$, was designated as CuNT.

2.2. Sample characterization

The prepared TiO$_2$ specimens were characterized by X-ray diffraction (XRD, BruckerAxs D8″ Advance, Germany) using a Cu Kα_1 source (λ = 0.15404 Å). Fourier transform infrared (FT-IR) spectrum was recorded by FTIR spectroscopy (Jasco FTIR 4100 spectrometer (Japan)). Raman spectroscopy was conducted on a Bruker instrument (Model Sentera, Germany), at laser wave length 532 nm [doubled Nd:YAG laser] with power ten mW. The scanning electron microscopy (SEM) images were carried out on a JEOL-JSM-6510 LV using a 15 kV in secondary electron mode. The morphology patterns of the investigated samples were observed using transmission electron microscope (JEM-2100CX JEO) with an acceleration voltage up to 200 kV, magnification power up to 600 kX and resolution power down to 0.2 nm. N$_2$ adsorption–desorption isotherms of the tested specimens were obtained at 77 K using a Quantachrome NOVA instrument. BET-surface areas were evaluated from the BET plots in 0.05–0.35 partial pressure range. Pore volumes and average pore diameters were obtained by using Barrett–Joyner–Halenda (BJH) model from the desorption isotherms. The diffuse reflectance spectra of the samples over a range of 200–800 nm were recorded using JASCO V-530 spectrometer (Japan). As a reference material, BaSO$_4$ was utilized. Photoluminescence (PL) spectra were recorded at room temperature on LS55 spectrofluorometer (Perkin Elmer, USA). Zeta-potential, as a function of the solution pH, was operated to decide the iso-electric point of the tested sample. The solution pH was regulated with 0.01 M NaOH or 0.01 M HCl. The fresh-prepared slurry of CuNT (0.1 g/L) was agitated for 20 min at 150 r/min until a stable ζ potential was attained.

2.3. Photocatalysis study

Methyl orange (MO) and Methylene blue (MB) are two familiar dyes, widely utilized in several applications. Therefore, we have chosen them as a type waste product to calculate the photocatalytic degradation over the investigated catalysts under UV and visible light irradiation. The degradation reactions were carried out using 3×10^{-5} M aqueous dye solutions. After adding 0.1 g titania catalysts and before lighting, the suspension was magnetically agitated for three h in the dark to make sure the mixture had attained adsorption equilibrium. By making blank tests, no variations were observed in dye concentrations through irradiation without photocatalysts. After adsorption–desorption equilibrium, the zero time reading was chosen, and the suspended solution was then irradiated with a 30-W mercury lamp (for UV irradiation) or with a 500-W xenon lamp (as a visible light source upon blocking UV light by a 400 nm glass filter) for five h. The reactions were carried out in a 10 cm diameter reaction bottle located under the lamp in a light assembly room, and the gap between the

lamp and the solution surface was permanently 20 cm. To determine the dye concentration, 5 ml of the suspended reaction was removed periodically and centrifuged to isolate the photocatalysts from the solution. The concentration of the dye taken from the solution obtained was determined by UV absorbance spectrometer (Jasco V-550, Japan) at 665 nm and 450 nm for MO and MB, respectively. For analysis, calibration curves between optical absorbance vs. dye concentration with a correlation factor of 0.996 were constructed. Degradation efficiencies were computed according to the following:

$$Degradation\ efficiency = \frac{C^o_{dye} - C^t_{dye}}{C^o_{dye}} \qquad (1)$$

where C^t_{dye} and C^0_{dye} represent the concentrations of the dye at time t and 0, respectively.

Photoanode preparation and Photocurrent measurements:

The photoanodes were prepared by dispersing the powdered sample into a tert-butanol alcohol with the weight ratio of 1–5 and stirring for 4 h to form a paste. The paste was then put on fluorine doped tin oxide glass (FTO) to a thickness of ~15 μm and heated at 200 °C for three hours.

Photoelectrochemical (PEC) measurements of the pure and doped thin films were performed in a three-electrode reactor cell. The cell was filled with an electrolyte of 1 M KOH. A Pt wire served as the counter electrode, and a saturated calomel electrode (SCE) used as the reference electrode. All electrodes were conducted to a potentiostat system (PGSTAT204) for the PEC measurements. The 1 cm^2 working electrode was illuminated with a 500-W xenon lamp. The measured light irradiance was 100 mW/cm^2. For visible-light illumination, the light was passed through an optical filter, which cut off wavelengths below 400 nm.

2.4. Determination of percentage mineralization

The reduction of chemical oxygen demand (COD) was selected as a key parameter of the organic matter degradation, which is subject to oxidation by a strong oxidant. The dichromate reflux method was adjusted to determine COD (Moore et al., 1951). The percent of mineralization was given by Tantak and Chaudhari (2006):

$$\%mineralization = \left[\frac{(COD_o - COD_t)x100}{COD_o}\right] \qquad (2)$$

where $COD_0 = COD$ of original dye, $COD_t = COD$ of degraded dye after time 't.'

3. Results and discussion

3.1. XRD

XRD patterns of the pure and doped TiO$_2$ specimens are illustrated in Fig. 1. The as-prepared pure sample showed (101), (004), (200), and (211) peaks at 2 values of 25.44, 37.68, 48.32, and 55.2°, indicating that the as-prepared pure TiO$_2$ has an anatase crystal structure according to JCPDS-21-1272. The CuT and CuNT doped samples showed small CuO (tenorite) diffraction peaks near $2\theta = 35.63°$ and 38.95°, indexed to the X-ray diffraction planes (−111) and (111) (PDF 41-0254). XRD of all the doped samples also showed that the peak positions of the obtained anatase
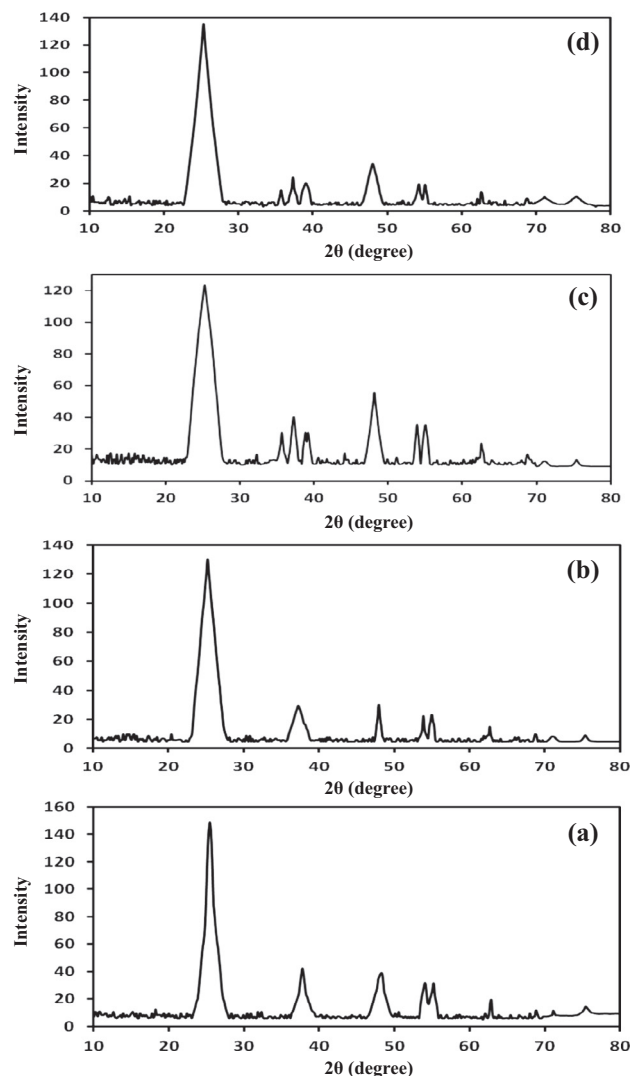

Fig. 1 XRD patterns of (a) T; (b) NT; (c) CuT and (d) CuNT.

structure are shifted a slightly toward the left as compared with that of pure anatase TiO$_2$. This shift refers to the incorporation of doped ions into the anatase TiO$_2$ besides some CuO phases formed on the surface of TiO$_2$. The crystallite sizes of the specimens were estimated from full-width at half-maximum of the (101) anatase peak (3) by the Debye-Scherrer equation (Klug and Alexander, 1970):

$$D_{XRD} = \frac{k\lambda}{\beta\cos\theta} \qquad (3)$$

where d represents the crystallite size; λ represents the X-ray wavelength; θ represents the Bragg angle and β is the diffraction peak width at half of the maximum intensity. The results obtained are recorded in Table 1. It is observed that the addition of dopant into TiO$_2$ caused a considerable decrease in the crystallite size. of TiO$_2$.

3.2. FTIR

FT-IR spectra of the specimens investigated were studied at a wavenumber of 400–4000 cm^{-1}. The results obtained are rep-

Table 1 Particle size, surface parameters and energy gap of the investigated samples.

Sample	D_{XRD} (nm)	D_{TEM} (nm)	S_{BET} (m²/g)	Pore diameter (nm)	Pore volume (ml/g)	E_g (eV)
T	16	17	151	41	0.25	3.04
CuT	11	12	253	35	0.45	2.46
NT	14	15	383	43	0.44	2.42
CuNT	10	9	375	38	0.54	2.3
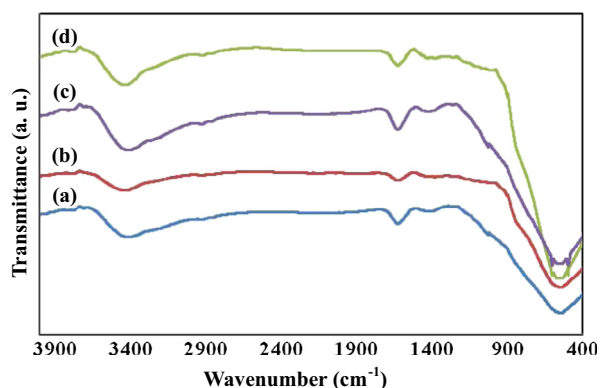
Fig. 2 FTIR spectra of (a) T; (b) NT; (c) CuT and (d) CuNT.
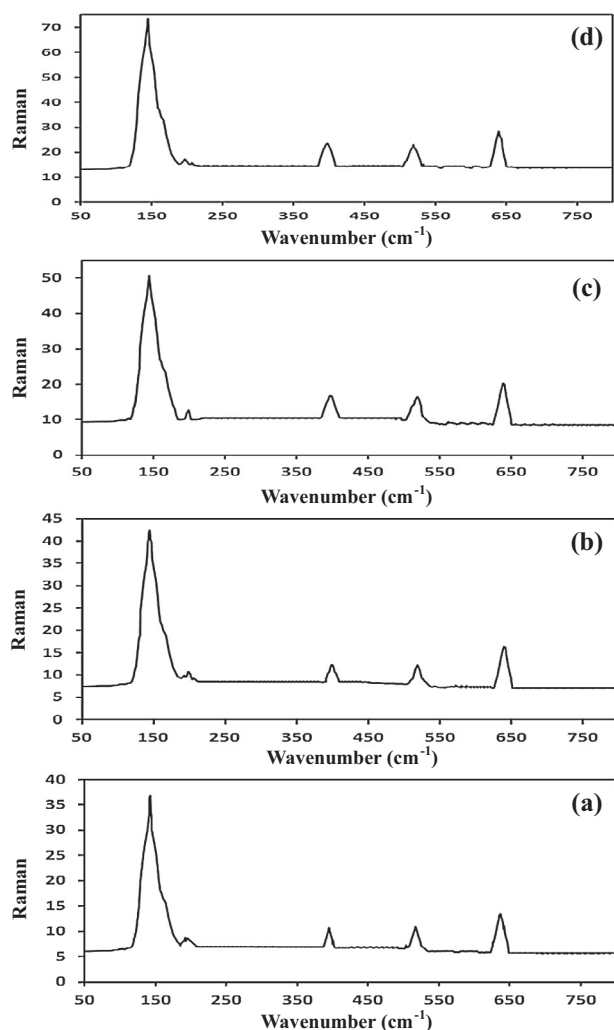
Fig. 3 Raman spectra of (a) T; (b) NT; (c) CuT and (d) CuNT.
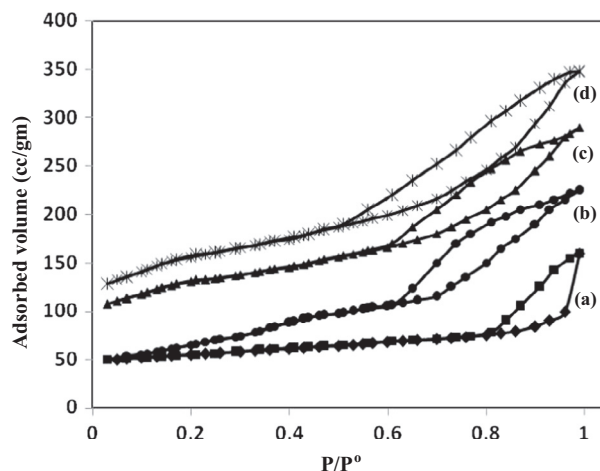
Fig. 4 N₂ adsorption-desorption isotherms of (a) T; (b) CuT; (c) NT; and (d) CuNT.

resented in Fig. 2. The peak observed in the range of 3740–3000 cm⁻¹ is attributed to O—H stretching vibration and the peak detected at 1524–1691 cm⁻¹ is assigned to O—H bending. All samples showed a clear absorbance band for the stretching vibration of Ti—O—Ti bond in the range of 400–800 cm⁻¹ (Wu et al., 2010). In contrast to the undoped TiO₂ each of NT and CuNT doped TiO₂ samples showed additional absorbance peaks at 1471, 1252 and 1082 cm⁻¹ assigned to the vibration of the Ti—N bond (Huo et al., 2009). The appearance of new bands below 1000 cm⁻¹ in the samples containing Cu is revealed to the vibration bond of Cu—O (Wang et al., 2009). These results confirmed that both the N and Cu species had been incorporated into the TiO₂ lattice.

3.3. Raman spectra

The structural belongings of the tested samples were extra studied by Raman spectroscopy. The spectra (Fig. 3) showed that the crystal structure of all the pure and doped specimens are existing in the anatase phase, linking to four distinguishing peaks with the main one detecting around 143 cm⁻¹ (Yang et al., 2010), which agrees well with the results obtained from XRD. The shift in the position of the principal peak of the doped samples toward higher wavenumber ∼144 cm⁻¹ indicates that the dopants may extend some defects and/or surface oxygen vacancies in the doped samples (Stella et al., 2016).

3.4. Textural properties

The surface area, pore size and total pore volume of specimens were concluded from the analyses of BET measurements. Nitrogen adsorption–desorption isotherm curves of the investigated
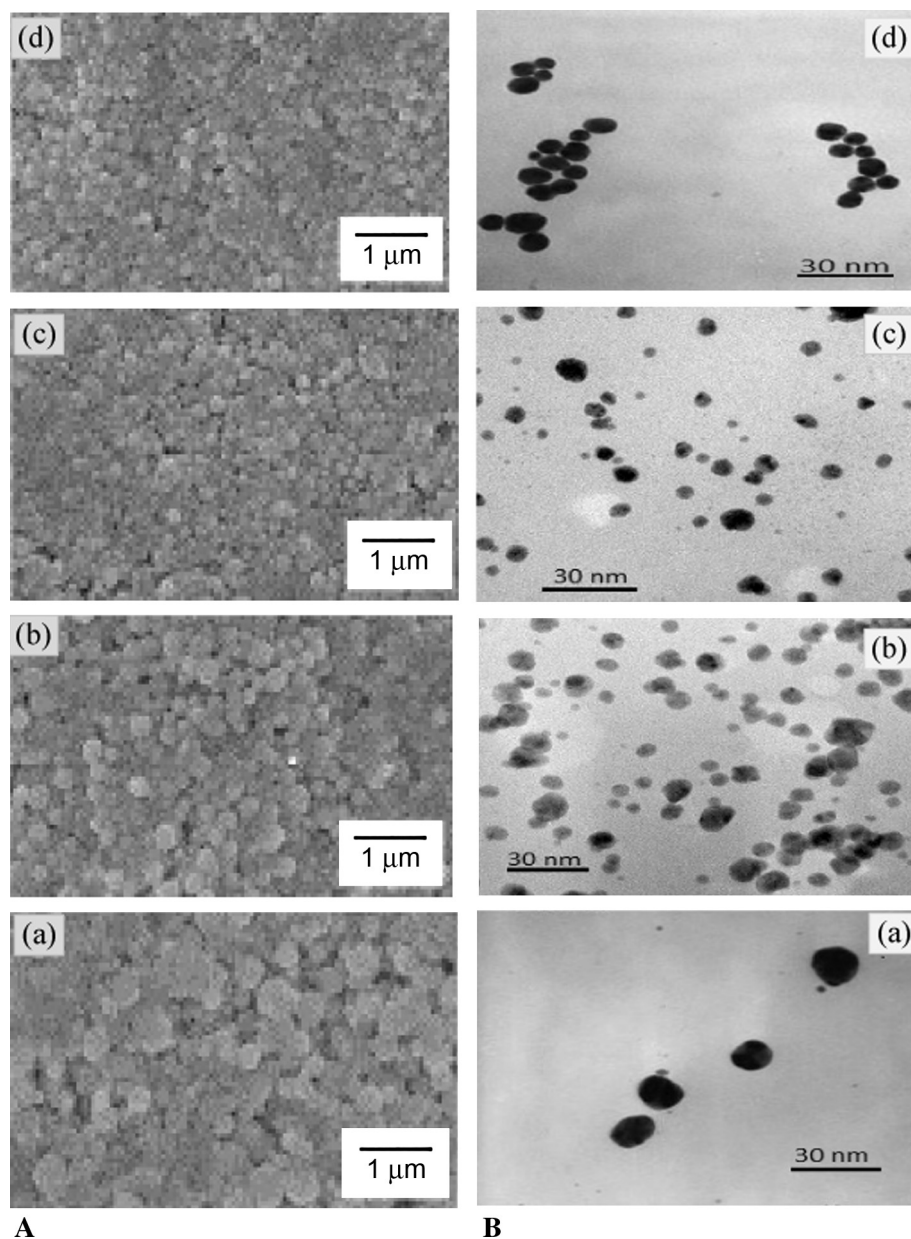
Fig. 5 (A) SEM micrographs of (a) T; (b) NT; (c) CuT and (d) CuNT. (B) TEM micrographs of (a) T; (b) NT; (c) CuT and (d) CuNT.

samples showed the type IV isotherms according to IUPAC classification, Fig. 4. This reveals to that all the samples exhibit a mesoporous structure. The pore size is analyzed by BJH method and listed with the other textural properties in Table 1, From which, it can be seen that the introducing of dopants into TiO_2 causes an enlargement in surface area. The surface area S_{BET} is ranked as follows: S_{BET} of NT: 383 $m^2/g/ > S_{BET}$ of NCuT: 375 $m^2/g > S_{BET}$ of CuT:253 $m^2/g > S_{BET}$ of T: 151 m^2/g. The increase in the surface area of the doped TiO_2 may be attached to that doping ions providing extra nucleation locations throughout the preparation process. Table 1 also shows that the investigated samples have mesoporous pore size and the pore diameter increases in the following sequence: NT > T > CuNT > CuT.

3.5. SEM and TEM

The morphological structure and particle size of the as-prepared TiO_2 samples were determined from SEM and TEM images shown in Fig. 5a and b. TEM analysis showed that all the samples have almost spheroid morphological structure. This uniform morphological structure might be attributed to using the microwave in the heating process (Komarneni et al., 1988). Mean particle diameters of 9, 12, 15, and 17 were monitored for specimens CuNT, CuT, NT, and T, respectively. The particle sizes obtained from TEM analyses agree well with those found in XRD results.
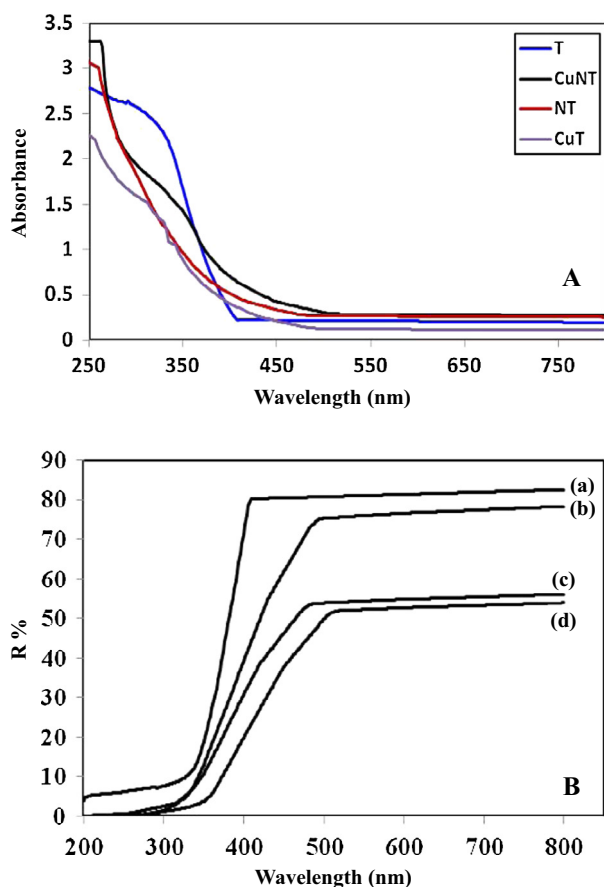
Fig. 6 (A) UV-vis absorption spectra of T, CuT, NT and CuNT. (B) Reflectance spectra of (a) T; (b) CuT; (c) NT and (d) CuNT samples.
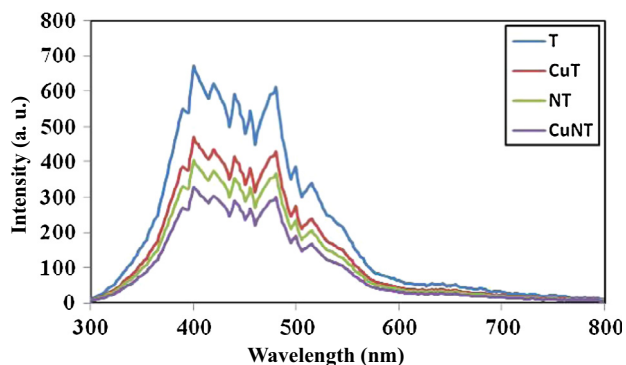

Fig. 7 Photoluminescence spectra of T, CuT, NT and CuNT.

3.6. UV-vis diffuse reflectance spectra (UV-vis-DRS)

Fig. 6 shows the UV-vis-DRS of all the samples under investigation. A red shift in the optical reflection edge was observed as a result of introducing doping ions into TiO₂ lattice. This shift reveals that the doping ions decrease the band gap energy of TiO₂ (Morikawa et al., 2001). The improved light absorption occurring in the doped samples can thus excite extra photon-generated carriers from the sample surface to degrade the organic contaminants in water, enabling the reasonable
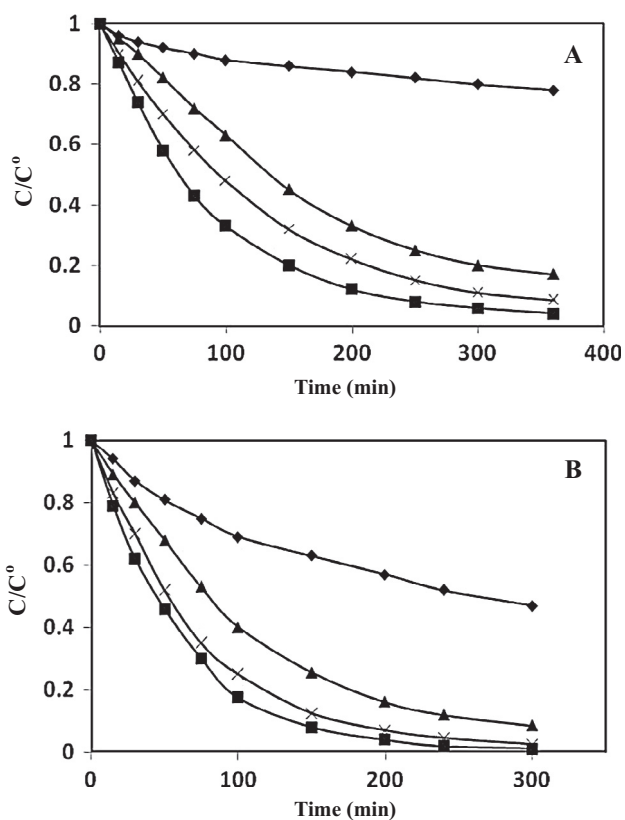

Fig. 8 Photocatalytic degradation of MB dye on T ($\blacklozenge$); CuT ($\blacktriangle$); NT ($\times$) and CuNT, ($\blacksquare$) samples under (A) visible light irradiation and (B) UV irradiation.

treatment under daylight. Among the doped TiO₂ samples, CuNT sample has the highest absorption in the visible light range. The indirect band gap (E_g) for the samples investigated was estimated from Tauck plots (Diamandescu et al., 2013), by plotting $[\alpha h\nu]^{0.5}$ vs. $h\nu$. The E_g values obtained are listed in Table 1 and found to be 3.04, 2.42, 2.46 and 2.3 eV for T, NT, CuT and CuNT samples, respectively. The indirect band gap value estimated for the pure specimen is near to that found for the anatase TiO₂ phase (3.2 eV) reported in the literature (Hong et al., 2005). In general, the considerable increase in the visible light absorption is attributed to the creation of new energy levels in the band-gap range due to the addition of doped ions. This agrees with earlier reports in the literature that Cu ion incorporation provides d-orbitals just below the conduction band which lowers the band gap energy (Park et al., 2013; Khan and Kim, 2009; Xiao et al., 2008).

3.7. Photoluminescence spectra (PL)

The photoluminescence emission spectra (PL) of the pure and doped TiO₂ samples have been studied to understand the separation and recombination of electron-hole pairs processes and the efficiency of charge-carrier transfer. In the present work, the PL emission spectra of the investigated samples are displayed in Fig. 7. It shows a major peak at around 398 nm, which is assigned to the band-to-band recombination because it is near -band-edge luminescence (Pugazhenthiran et al., 2013). The spectrum of pure TiO₂ also shows other small PL
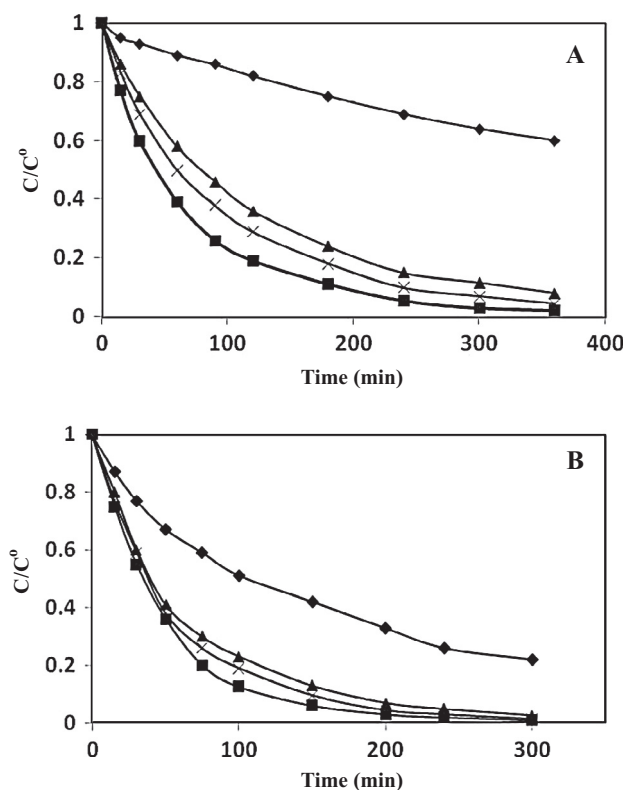
Fig. 9 Photocatalytic degradation of MO dye on T (◆); CuT (▲); NT (×) and CuNT, (■) samples under (A) visible light irradiation and (B) UV irradiation.

peaks at wavelengths between 420 nm and 500 nm, which are attributed to the transition from localized surface states to the valence band of TiO_2 (Pugazhenthiran et al., 2013). The peaks appeared in PL spectra of the doped TiO_2 are almost observed at the same locations of those found in pure TiO_2, but with a drop in their intensities. This refers to the inhibition occurring in photo-generated electron recombination from the conduction band to valence band of TiO_2. The higher PL peak intensity recorded for undoped TiO_2 refers to the reduction in the electron–hole lifetime owing to the fast recombination rate. The highest reduction in PL intensity in CuNT sample reveals its top effectiveness of the investigated samples on reducing the recombination rate of photo-generated electron–hole process in TiO_2 (Ni et al., 2007).

3.8. Photocatalytic activity study

The photocatalytic degradation of MB and MO aqueous solutions was investigated under UV and visible light irradiations.

The degradation ratios (C/C^0) of MB and MO as a function of time for the samples investigated are represented in Figs 8 and 9. All the doped-TiO_2 photocatalysts showed enhanced activities about pure TiO_2. The results summarized in Table 2 show that, under the irradiation in the UV and visible ranges, the photocatalytic performance of anatase TiO_2 is improved by the presence of the dopant ions. However, the catalyst activity is dependent on the dopant type.

Also, in this work, it was important to determine the kinetic law for the photocatalytic process. Figs. 10 and 11 show the plots of (ln C/C^0) vs. time (t) for the dye degradation reactions under UV and visible light irradiation. The plots demonstrated straight lines, and from their slopes the apparent first-order rate constants (k_{app}) and the square correlation factors R^2 were evaluated and are listed in Table 3. The first-order kinetics for both MO and MB Photocatalyzed degradation has also been established by other authors (Mukhlish et al., 2013; Mahmoodi, 2014).

Based on the photocatalytic activity results, the best performing CuNT material was further investigated to optimize the photodegradation rate, through measuring the degradation efficiency as a function of different experimental parameters (pH, catalyst dosage, dye concentration). Moreover, the surface charge of CuNT was tested by measuring Zeta potential as a function of pH (Fig. S1) due to the importance of pollutant adsorption on the sample surface that is dependent on the medium acidity (Reynoso-Soto et al., 2013). For pH values smaller than 6 the surface is positively charged, while it flips to negative charges for pH values greater than 6.

The influence of pH on the degradation rate of MO and MB was investigated in the range 2.0–10.0 as illustrated in Fig. S2. It was found that the photocatalytic degradation rate of MO increases with pH to attain a maximum value at pH = 6 and then decreases. This is because, in acidic solution, TiO_2 samples are positively charged which adsorbs MO molecules by electrostatic attraction, whereas, in alkaline solution, TiO_2 is negatively charged and the adsorption of MO molecules is weak due to repulsive forces (Wang et al., 2014). On the other hand in the case of MB, pH = 9 was found to be the optimum condition for the MB degradation. This is attributed to that at higher pH the surface of TiO_2 is negatively charged and adsorbs MB (cationic dye) by the electrostatic force (Dhananasekaran et al., 2016).

The effect of dye concentration on the photodegradation rate was also studied, and the results are shown in Fig. S3. The degradation rate was found to rise with increasing the dye concentration up to 2.0×10^{-5} M and 3.0×10^{-5} M for MB and MO, respectively. This can be explained on the basis that by increasing the dye concentration, more dye molecules were available for excitation and succeeding energy/electron transfer and hence, an increase in the dye degradation rate

Table 2 Degradation ratio (C/C^0) at $t = 2$ h under visible light and UV irradiation for MB and MO by pure and doped TiO_2 samples.

Sample	Visible light irradiation		UV irradiation	
	MB	MO	MB	MO
T	0.87	0.82	0.66	0.47
CuT	0.55	0.36	0.34	0.18
NT	0.41	0.29	0.19	0.13
CuNT	0.27	0.19	0.13	0.09

Fig. 10 Kinetic studies of photocatalytic degradation of MB dye on T (♦); CuT (▲); NT (×) and CuNT, (■) samples under (A) visible light irradiation and (B) UV irradiation.
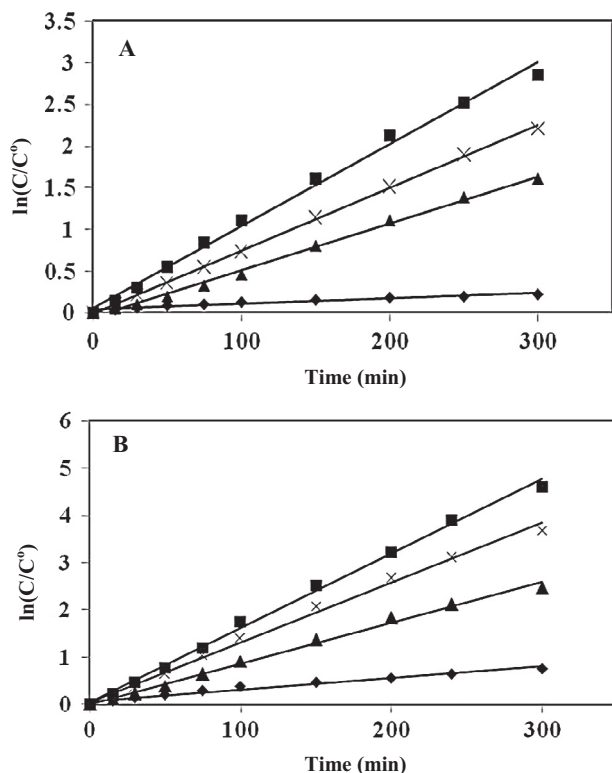

Fig. 11 Kinetic studies of photocatalytic degradation of MO dye on T (♦); CuT (▲); NT (×) and CuNT, (■) samples under (A) visible light irradiation and (B) UV irradiation.
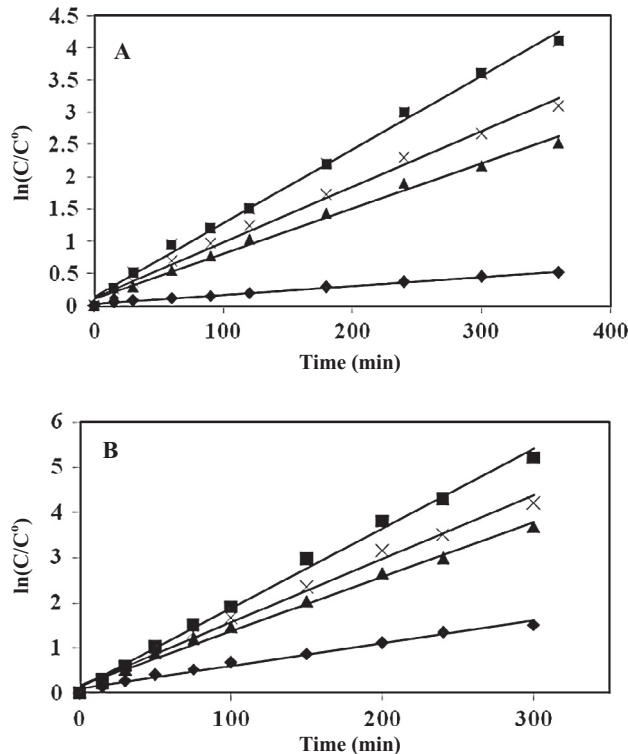
was observed. On increasing the concentration of dye above the mentioned optimum concentrations, the degradation rate decreases. This is because, after a particular concentration, the dye acts as a blocking layer thus decreasing the delivered light intensity to the photocatalyst surface.

The photocatalyst dosage may also affect the degradation of dyes and thus different amounts of CuNT photocatalyst were tested. The results are represented in Fig. S4. By increasing the amount of photocatalyst, the rate of reaction was found to increase and attain an optimum value at 0.14 g. This is because as the catalyst amount increases, more active sites become available to adsorb extra amount of dye molecules. Above 0.14 g, the degradation rate becomes nearly constant. This is due to that the increase in the photocatalyst dosage will only increase the thickness of the layer of the catalyst and not its exposed surface area.

The increase in the photocatalytic activity of the doped TiO$_2$ samples relative to the pure one can be interpreted based on the formation of new energy levels by the dopants and the lifetime of the electron-hole pairs produced by the light irradiation. In the case of pure TiO$_2$, the particles take up the light that matches its band gap energy thus moving an electron from the valence band to its conduction band, creating electron–hole charge separation. These charges join with each of surface hydroxyl groups and oxygen adsorbed on TiO$_2$ surface, forming oversensitive oxygen types, that react with the dyes causing their degradation. On the other hand, in the case of NT sample the introduction of nitrogen into TiO$_2$ lattice produces a midgap (N 2p) level, that is created to some extent over the top of the (O 2p) valence band Yang et al., 2010. And in the case of CuT sample the introduction of Cu^{2+} with a valency state less than that of Ti^{4+} will produce oxygen vacancies acting as energetic locations for dye dissociation on the TiO$_2$-surface. For the dye degradation process to proceed, the producing electron and hole lifetimes must be long enough. This will give more chance for the created charges to attain the photocatalyst surface to react with the adsorbed dye. In the cases of the doped samples, the produced photo generated electrons will be trapped by the induced defects produced in the TiO$_2$ lattice. This leads to an increase in the electron-hole pair lifetime, and hence increasing the possibility of reactions between the created electron–hole pairs and adsorbed species on the surface of the catalyst (Buchalska et al., 2015).

The quantum efficiencies of the photocatalytic degradation of MO and MB for CuNT were determined using photon flux of visible light 2.01×10^{-5} einstein/s. After two h of the illumination, the efficiency was calculated to be 2.1×10^{-5} moles/ Einstein.

3.9. Photocurrent measurement

In order to characterize the different sample's ability of separating of photogenerated electrons and producing charge carriers, a series of the PEC experiments were conducted. Fig. 12(a) and (b) shows the plots of J_{ph} versus bias potential (V) of all studied samples under illumination of a 100 mW/ cm^2 Xe lamp without and with a UV cutoff filter. The dark current densities of each sample showed a very small value within the whole bias potential range. Under both UV and visible light illuminations, all the samples produced photocurrent significantly higher than the dark current. Besides, all samples

Table 3 Kinetic parameters for degradation of MB and MO over tested samples under visible as well as UV light irradiation.

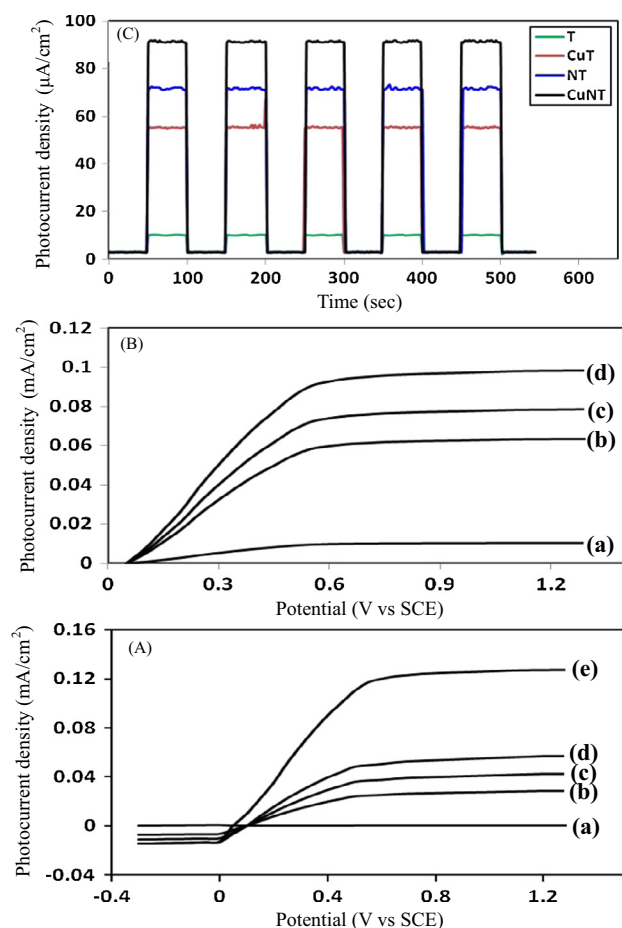| Sample	Visible light irradiation				UV irradiation			
	MB		MO		MB		MO	
	k_{app} (min^{-1})	R^2	k_{app} (min^{-1})	R^2	k_{app} (min^{-1})	R^2	k_{app} (min^{-1})	R^2
T	7.0×10^{-4}	0.937	1.4×10^{-3}	0.996	2.5×10^{-3}	0 0.975	5×10^{-3}	0.987
CuT	5.6×10^{-3}	0.996	7.0×10^{-3}	0.993	8.6×10^{-3}	0.994	1.2×10^{-2}	0.992
NT	7.5×10^{-3}	0.999	8.6×10^{-3}	0.994	1.3×10^{-2}	0.996	1.4×10^{-2}	0.992
CuNT	9.8×10^{-3}	0.994	1.1×10^{-2}	0.996	1.6×10^{-2}	0.997	1.8×10^{-2}	0.995

Fig.12 (A) Photocurrent-applied potential (vs. SCE) curve under UV-irradiation of (a) T (dark); (b) CuNT; (c) NT; (d) CuT and (e) T. (B) Photocurrent-applied potential (vs. SCE) curve under visible irradiation of (a) T; (b) CuT; (c) NT and (d) CuNT and (C) photocurrent intensity at 0.5 V of T, NT, CuT and CuNT photoanodes.

Fig. 13 Mineralization percent of MO on CuNT sample.

show a higher increase in the photocurrent with applied potential. Additionally, the transient photocurrent measured at fixed bias voltage of 0.5 V vs. SCE with a visible light pulse 50 s, was studied and the results obtained are represented in Fig.12c. It can be seen that the responses of the photocurrent were reproducible during the repeated on-off cycles. Also, the J_{ph} values of the studied samples, under visible illumination, increase according to CuNT > CuT > NT > T. These results go in a parallel way with that obtained in photocatalytic results and imply that under visible light illumination, photocatalysts are
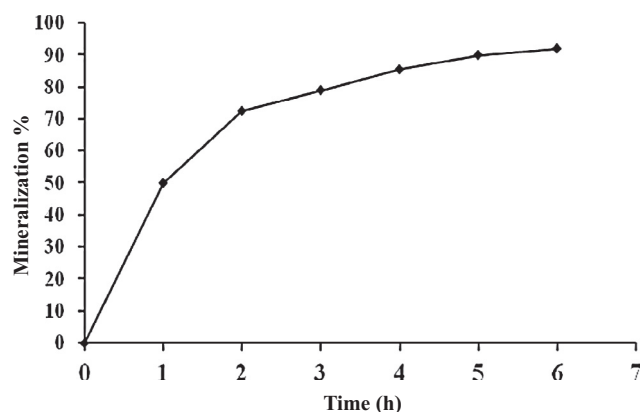
excited to form the photogenerated electron-hole pairs, where Cu and N codoping of TiO_2 tends to easily produce charge carriers and separate electrons under visible illumination source

3.10. Mineralization of dyes

The measurement of the fall in the chemical oxygen demand (COD) of irradiated solutions is usually used to monitor the mineralization of dyes. With initial MO concentration of 3.2×10^{-4} mol L^{-1} and catalyst load 0.14 g L^{-1}, a fixed reduction in COD with the enlargement in the irradiation time was noted (Fig. 13). The percentage mineralization of MO increased with irradiation time to reach a value of 95.14% after six h. Furthermore, the percentage mineralization was less (73%) compared to percentage decolorization (96.24%). The production of smaller uncoloured products during the decolorization process might be responsible for comparatively higher values of COD, which could not impart any color, showing a higher percentage of decolorization.

4. Conclusions

N, Cu, and N, Cu-codoped TiO_2 nanoparticle catalysts were synthesized by a microwave-assisted sol-gel process. All the samples showed an anatase TiO_2 phase structure with spherical particles exhibiting size in the range of 9–17 nm and surface with a mesoporous structure. The doped TiO_2 samples exhibited higher surface area (253–383 m^2/g) than that of pure one (151 m^2/g) and showed a better light harvesting in both visible light and UV and regions with a decrease in the band gap energies relative to that of pure TiO_2. The influence of dye acidity on the photocatalytic degradation rates of the studied materials was investigated using methylene blue (cationic dye) and methyl orange (azo dye). The dissimilar activity degrees of the photocatalysts for both

dyes showed that the catalytic efficiency of the samples clearly differed with the kind of dopant used. Amon all the photocatalysts, (Cu,N)-codoped TiO$_2$ (CuNT) sample showed the highest photocurrent and catalytic efficiency under visible light for MB and MO due to the small band gap energy and prolonged electron–hole recombination. The presented low-cost doped material (CuNT) has good capabilities of high-throughput treatment of wastewater under visible light range.

Appendix A. Supplementary material

Supplementary data associated with this article can be found, in the online version, at http://dx.doi.org/10.1016/j.arabjc.2017.02.002.

References

Ashkarran, A.A., 2011. Antibacterial properties of silver-doped TiO$_2$ nanoparticles under solar simulated light. J. Theoret. Appl. Phys. 4, 1–8.

Buchalska, M., Kobielusz, M., Matuszek, A., Pacia, M., Wojtyła, S., Macyk, W., 2015. On oxygen activation at rutile- and anatase-TiO$_2$. ACS Catal. 5, 7424–7431.

Dhananasekaran, S., Palanivel, R., Pappu, S., 2016. Adsorption of methylene blue, bromophenolblue, and coomassiebrilliant blue by α-chitin nanoparticles. J. Adv. Res. 7, 113–124.

Diamandescu, L., Vasiliu, F., Tarabasanu-Mihaila, D., Feder, M., Vlaicu, A.M., He, K., Hong, R.Y., Feng, W.G., Badami, D., 2013. A facile co-precipitation synthesis of hexagonal (Zn, Mg)TiO$_2$. Powder Technol. 239, 518–524.

Dong, H., Zeng, G., Tang, L., Fan, C., Zhang, C., He, X., He, Y., 2015. An overview on limitations of TiO$_2$-based particles for photocatalytic degradation of organic pollutants and the corresponding countermeasures. Water Res. 79, 128–146.

Hong, Y.C., Uk Bang, C., Shin, D.H., Uhm, H.S., 2005. Band gap narrowing of TiO$_2$ by nitrogen doping in atmospheric microwave plasma. Chem. Phys. Lett. 413, 454–457.

Huo, Y., Jin, Y., Zhu, J., Li, H., 2009. Highly active TiO$_{2-x-y}$N$_x$F$_y$ visible photocatalyst prepared under supercritical conditions in NH$_4$F/EtOH fluid Appl. Catal. B 89, 543–550.

Khan, R., Kim, T.J., 2009. Preparation and application of visible-light-responsive Ni-doped and SnO$_2$-coupled TiO$_2$ nanocomposite photocatalyst. J. Hazard. Mater. 163, 1179–1184.

Klug, H.P., Alexander, L.E., 1970. X-ray Diffraction Procedures. Wiley, New York.

Komarneni, S., Breval, E., Roy, R., 1988. In: Sutton, W.H., Brooks, M.H., Chabinsky, I.J. (Eds.), Microwave Processing of Materials, J. Mater. Research So., Pittsburgh, 124, pp. 235–238.

Kumar, S.G., Devi, L.G., 2011. Review on modified TiO$_2$ photocatalysis under UV/Visible light: selected results and related mechanisms on interfacial charge carrier transfer dynamics. J. Phys. Chem. A 115, 13211–13241.

Mahmoodi, N.M., 2014. Binary catalyst system dye degradation using photocatalysis. Fibers Polym. 15, 273–280.

Moore, W.A., Ludzack, F.J., Ruchhoft, C.C., 1951. Determination of oxygen-consumed values of organic wastes. Anal. Chem. 23, 1297.

Morikawa, T., Asahi, R., Ohwaki, T., Aoki, K., Taga, Y., 2001. Band-gap narrowing of titanium dioxide by nitrogen doping. J. Appl. Phys. 40, L561.

Mukhlish, M.Z.B., Najnin, F., Rahman, M.M., Uddin, M.J., 2013. Photocatalytic degradation of different dyes using TiO$_2$ with high surface area: a kinetic study. J. Sci. Res. 5, 301–314.

Ni, Meng, Michael Leung, K.H., Dennis, Y.C., Sumathy, K., 2007. A review and recent developments in photocatalytic water-splitting using TiO$_2$ for hydrogen production. Renew. Sustain. Energy Rev. 11, 401–425.

Park, J., Choi, K., Lee, J., Hwang, C., Choi, D., 2013. Fabrication and characterization of metal-dopedTiO$_2$ nanofibers for photocatalytic reactions. Mater. Lett. 97, 64–66.

Pugazhenthiran, N., Murugesan, S., Anandan, A., 2013. High surface area Ag-TiO$_2$ nanotubes for solar/visible light photocatalytic degradation of ceftiofur sodium. J. Hazard Mater. 263, 541–549.

Reynoso-Soto, E.A., Pérez-Sicairos, S., Reyes-Cruzaley, A.P., Castro-Riquelme, C.L., María Félix-Navarro, R., Paraguay-Delgado, F., Alonso-Núñez, G., Lin-Ho, S.W., 2013. Photocatalytic degradation of nitrobenzene using nanocrystalline TiO$_2$ photocatalyst doped with Zn ions. J. Mex. Chem. Soc. 57, 298–305.

Schneider, J., Matsuoka, M., Takeuchi, M., Zhang, J., Horiuchi, Y., Anpo, M., Bahnemann, D.W., 2014. Understanding TiO$_2$ photo-catalysis: mechanisms and materials. Chem. Rev. 114, 9919–9986.

Stella, C., Prabhakar, D., Prabhu, M., Soundararajan, N., Ramachan-dran, K., 2016. Oxygen vacancies induced room temperature ferromagnetism and gas sensing properties of Co-doped TiO$_2$ nanoparticles. Mater. Electron. 27, 1636–1644.

Szkoda, M., Siuzdak, K., Lisowska-Oleksiak, A., 2016. On-metal doped TiO$_2$ nanotube arrays for high efficiency photocatalytic decomposition of organic species in water. Phys. E: Low-dimension. Syst. Nanostruct. 84, 141–145.

Tantak, N.P., Chaudhari, S., 2006. Degradation of azo dyes by sequential Fenton's oxidation and aerobic biological treatment. J. Hazard. Mater. B 136, 698–705.

Wang, S., Xu, H., Qian, L., Jia, X., Wang, J., Liu, Y., Tang, W., 2009. CTab-assisted synthesis and photocatalytic property of CuO hollow microspheres. J. Solid State Chem. 182 (2009), 1088–1093.

Wang, Y. Duan, W., Liu, Bo, Chen, X., Yang, F., Guo, J., 2014. The effects of doping copper and mesoporous structure on photocatalytic properties of TiO$_2$, J. Nanomater. 2014, pp. 7 (Article ID 178152).

Wang, Y., Zhang, R., Li, J., Li, L., Lin, S., 2014. First-principles study on transition metal-doped anatase TiO$_2$. Nanoscale Res. Lett. 9, 46.

Wei, L., Shi-Hao, W., Xiang-Mei, D., 2014. A strategy of enhancing the photoactivity of TiO$_2$ containing nonmetal and transition metal dopants. Chin. Phys. B 23, 027305.

Wu, M., Yang, B.F., Lv, Y., Fu, Z.P., Xu, J., Guo, T., Zhan, Y.X., 2010. Efficient one-pot synthesis of Ag nanoparticles loaded on N-doped multiphase TiO$_2$ hollow nanorod arrays with enhanced photocatalytic activity. Appl. Surf. Sci. 256, 7125–7130.

Xiao, Q., Si, Z., Yu, Z., Qiu, G., 2008. Characterization and photocatalytic activity of Sm^{3+} doped TiO$_2$ nanocrystalline prepared by low temperature combustion method. J. Alloys Comp. 450, 426–431.

Yang, X., Cao, C., Erickson, L., Hohn, K., Maghirang, R., Klabunde, K., 2009. Photo-catalytic degradation of Rhodamine B on C-, S-, N-, and Fe-doped TiO$_2$ under visible-light irradiation. Appl. Catal. B: Environ. 91, 657–662.

Yang, G., Jiang, Z., Shi, H., Xiao, T., Yan, Z., 2010. Preparation of highly visible-light active N-doped TiO$_2$ photocatalyst. J. Mater. Chem. 20, 5301–5309.

Yang, G., Jiang, Z., Shi, H., Xiao, T., Yan, Z., 2010. Preparation of highly visible-light active N-doped TiO$_2$ photocatalyst. J. Mater. Chem. 20, 5301–5309.

Zhai, C., Zhu, M., Lu, Y., Ren, F., Wang, C., Du, Y., Yang, P., 2014. Reduced grapheme oxide modified highly ordered TiO$_2$ nanotube arrays photoelectrode with enhanced photoelectrocatalytic performance under visible-light irradiation. Phys. Chem. Chem. Phys. 16, 14800–14807.

Zhu, M., Zhai, C., Qiu, L., Lu, C., Paton, A.S., Du, Y., Goh, M.C., 2015. New method to synthesize S-doped TiO$_2$ with stable and highly efficient photocatalytic performance under indoor sunlight irradiation. ACS Sustain. Chem. Eng. 3, 3123.